Combining Multicomponent Seismic Attributes, New Rock Physics Models, and In Situ Data to Estimate Gas-Hydrate Concentrations in Deep-Water, Near-Seafloor Strata of the Gulf of Mexico

PROJECT CONTINUATION REPORT

Reporting Period Start Date: 1 March 2006

Reporting Period End Date: 31 August 2007

Principal Investigators: Bob A. Hardage
Paul E. Murray
Diana C. Sava

Report Date: 13 June 2007

DOE Award DE-FC26-05NT42667

Submitting Organization: Bureau of Economic Geology
The University of Texas at Austin
University Station, Box X
Austin, TX 78713-8924

Disclaimer

Abstract

The gas hydrate research being done at the Bureau of Economic Geology through DOE Award DE-FC26-05NT42667 is now at its halfway point. The project is on schedule and on budget. The research objectives accomplished in the first half of the study include

1. selection of two deep-water hydrate study areas in the Green Canyon area of the Gulf of Mexico;
2. completion of a detailed research database of logs, multicomponent seismic data, geotechnical reports, and chirp-sonar profiles across these two study areas;
3. construction of a rock-physics theory that relates well log resistivities of deep-water sediments to hydrate concentrations;
4. development of a new seismic data-processing strategy that creates high-resolution P-P and P-SV images of deep-water, near-seafloor geology; and
5. application of this data-processing strategy in the preliminary processing of approximately 200 km of 4C ocean-bottom-cable seismic data.

These accomplishments are important in that (a) they document a new approach to estimating hydrate concentration from resistivity logs that is based on using the Hashin-Shtrikman Lower Bound to define the resistivity of a high-porosity, low-effective-pressure mixture of quartz grains, clay grains, hydrate, and brine, and (b) they show how multicomponent seismic data can be used to evaluate deep-water hydrate systems with both P-P and P-SV seismic attributes and with a resolution that cannot be achieved using towed-cable seismic data. We are convinced that our research findings will provide a valuable technology for others to use in future evaluation and exploitation of deep-water marine hydrates. We request a continuation of research funding for the second half of the project. This funding will allow us to finish our remaining research tasks and to complete our documentation of a new technology for studying deep-water, near-seafloor geology.

Table of Contents

List of Figures

Introduction

The Bureau of Economic Geology has completed all tasks that were scheduled to be done during the first 18 months of this project and has submitted all reports and deliverables that were due for the first half of the project period. Included in these deliverables were two special, decision-point reports requested by DOE. One of these special reports described the database that we amassed so that DOE could decide whether the database was appropriate for a hydrate research study. The second special report showed well log evidence confirming that hydrates exist at the sites selected for study. Principal research progress:

- New seismic data-processing concepts have been developed and tested confirming that four-component ocean-bottom-cable (4C OBC) seismic data provide better resolution of deep-water, near-seafloor strata than has yet been demonstrated by any previous research group (Backus and others, 2006);
- We have illustrated that near-seafloor geology can be interpreted using P-SV seismic images, sequences, facies, and attributes and that geological models of near-seafloor strata no longer have to be limited to information provided by only P-P seismic images, sequences, facies, and attributes; and
- Procedures for analyzing resistivity log data acquired across deep-water, near-seafloor strata have been developed that will allow log-based estimates of hydrate concentration to be used to calibrate seismic-based estimates of hydrate concentration (Hardage and others, 2006a).

Executive Summary

Our research activity in the first half of this project has focused on the three concepts that we used to construct the title of our research project:

1. <u>Multicomponent seismic attributes:</u> We developed a new concept for processing 4C OBC seismic data that allows deep-water, near-seafloor geology to be analyzed with both P-P and P-SV seismic attributes and with a resolution that has never been available using towed-cable seismic technology.
2. <u>New rock physics model:</u> We developed a rock physics model that relates log-based resistivity to estimates of hydrate concentration. This model uses the Hashin-Shtrikman Lower Bound to describe the resistivity of hydrate embedded in a host medium that has low (almost zero) effective pressure, excessive porosity (45 to 70 percent), and limited grain-to-grain contacts.
3. <u>In situ data:</u> We amassed geotechnical test data made on cores acquired across near-seafloor strata within our study areas, as well as all available well logs that were acquired across the hydrate stability zone within and near our study sites. Collectively these in situ data provide essential calibration data that we need to determine whether our seismic attributes

and our resistivity-log theory produce accurate estimates of hydrate concentration in deep-water environments (Hardage and others, 2006b).

Experimental

Work during the first half of this study involved the development of a theory that describes the propagation of P and S seismic wavefields in a medium consisting of arbitrary volume-fractions of hydrate, brine, quartz minerals, and clay minerals and a second theory that describes the electrical resistivity of this unique medium. These theoretical concepts were then converted into two functioning software codes: one code for processing seismic data and one code for analyzing resistivity log data. These two software codes were then applied to 4C OBC seismic data and to resistivity log data across our two selected study sites.

Results and Discussion

Task 1.0: Plan Research Management

This task had one deliverable—a report describing project objectives, approaches to achieving these objectives, schedules and planned expenditures for each research task, and all major milestones and decision points. That report was delivered to DOE and was accepted as a fulfillment of the deliverable.

Task 2.0: Assess Technology Status

This task had one deliverable—a report describing the current state of knowledge and technology relevant to the proposed research. That report was prepared, delivered to DOE, and accepted as an appropriate deliverable.

Task 3.0: Select Project Study Sites

We were required to do two things in this task: (1) select two deep-water study sites in the Gulf of Mexico (GOM) and (2) produce evidence that hydrates exist at each site. We selected the two sites labeled ***Area 1*** and ***Area 2*** on the map shown as Figure 1. These two study areas are at the southern edge (deepest water portion) of 4C OBC seismic surveys GCNC and GCNE in the Green Canyon area that were available for our analysis. A report documenting our research findings was delivered to DOE (Hardage and others, 2006a).

Two respected hydrate researchers, Dr. Harry Roberts (LSU) and Dr. Roger Sassen (Texas A&M), had documented the presence of hydrate at each site, and we used their research findings to justify these sites being appropriate for this study (Sassen and others, 1999; Roberts, 2001). In addition, we cited a previous DOE report documenting that hydrate was recovered from shallow cores at Study Site 1 (Brooks and Bryant, 1985). DOE did not consider the evidence published by Roberts, Sassen, and Brooks and Bryant to be sufficient and requested that additional log-based evidence of the presence of hydrate be provided. This request for log-based evidence of hydrate was added as a subtask to Task 4.0 that will be discussed next.

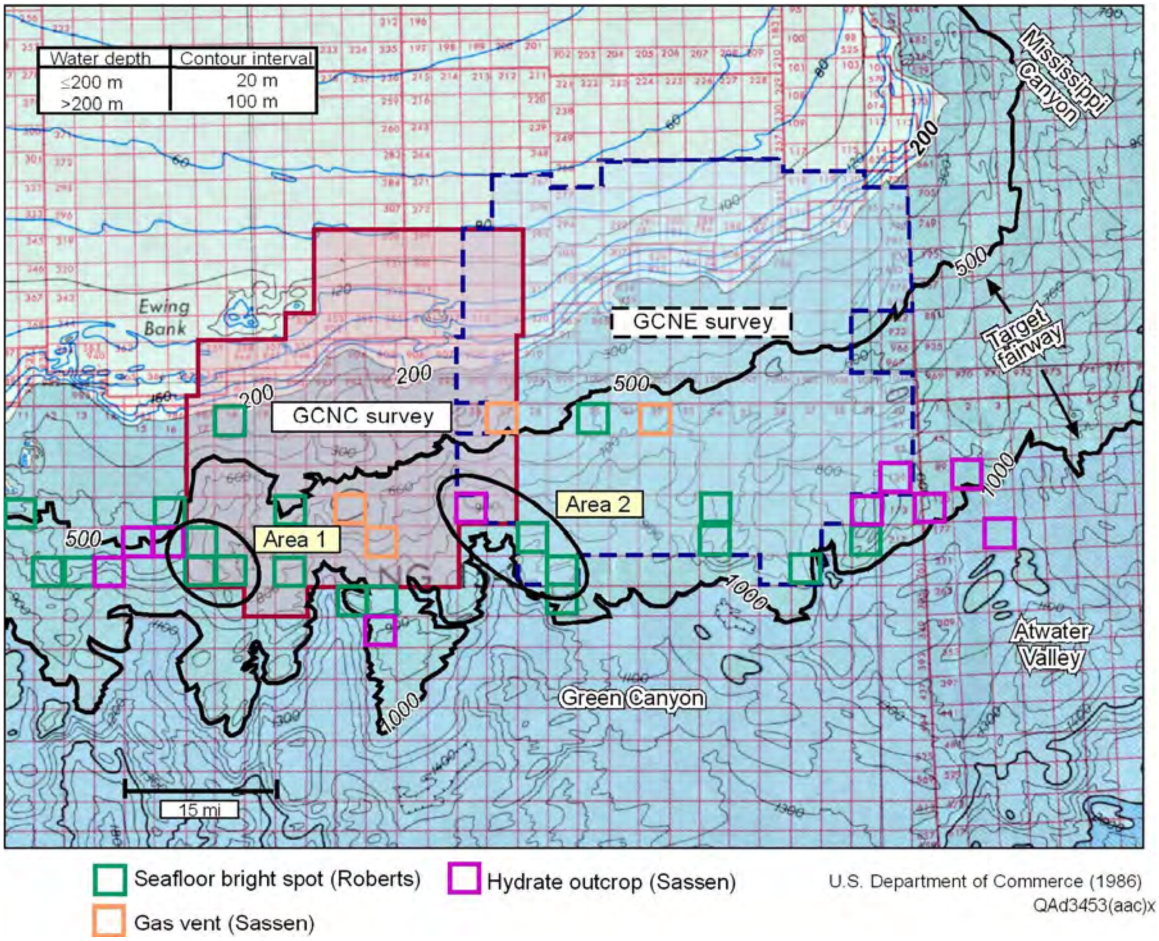

Figure 1. The two sites selected for this research are the circled areas labeled ***Area 1*** and ***Area 2***. Both sites are in water depths appropriate for GOM hydrate systems, and respected hydrate researchers Dr. Roger Sassen (1999) and Dr. Harry Roberts (2001) documented hydrate outcrops and other evidence of hydrate presence at each site.

Task 4.0: Build Database and Provide Subseafloor Evidence of Hydrate Presence

For this task, we amassed the databases that are summarized in Figure 2 for Study Site 1 and in Figure 3 for Study Site 2. The critical data amassed at each site consisted of north-south- and east-west-oriented 4C OBC seismic profiles spaced 2 miles apart, high-frequency (2–10 kHz) chirp-sonar data acquired along selected OBC profiles using Autonomous Underwater Vehicle (AUV) technology, geotechnical reports describing laboratory testing of near-seafloor cores taken where production platforms were set at Typhoon field (Fig. 2) and at Genesis field (Fig. 3), and all available well logs inside and near each study area that were acquired across shallow strata within the hydrate stability zone (Hardage and others, 2006c).

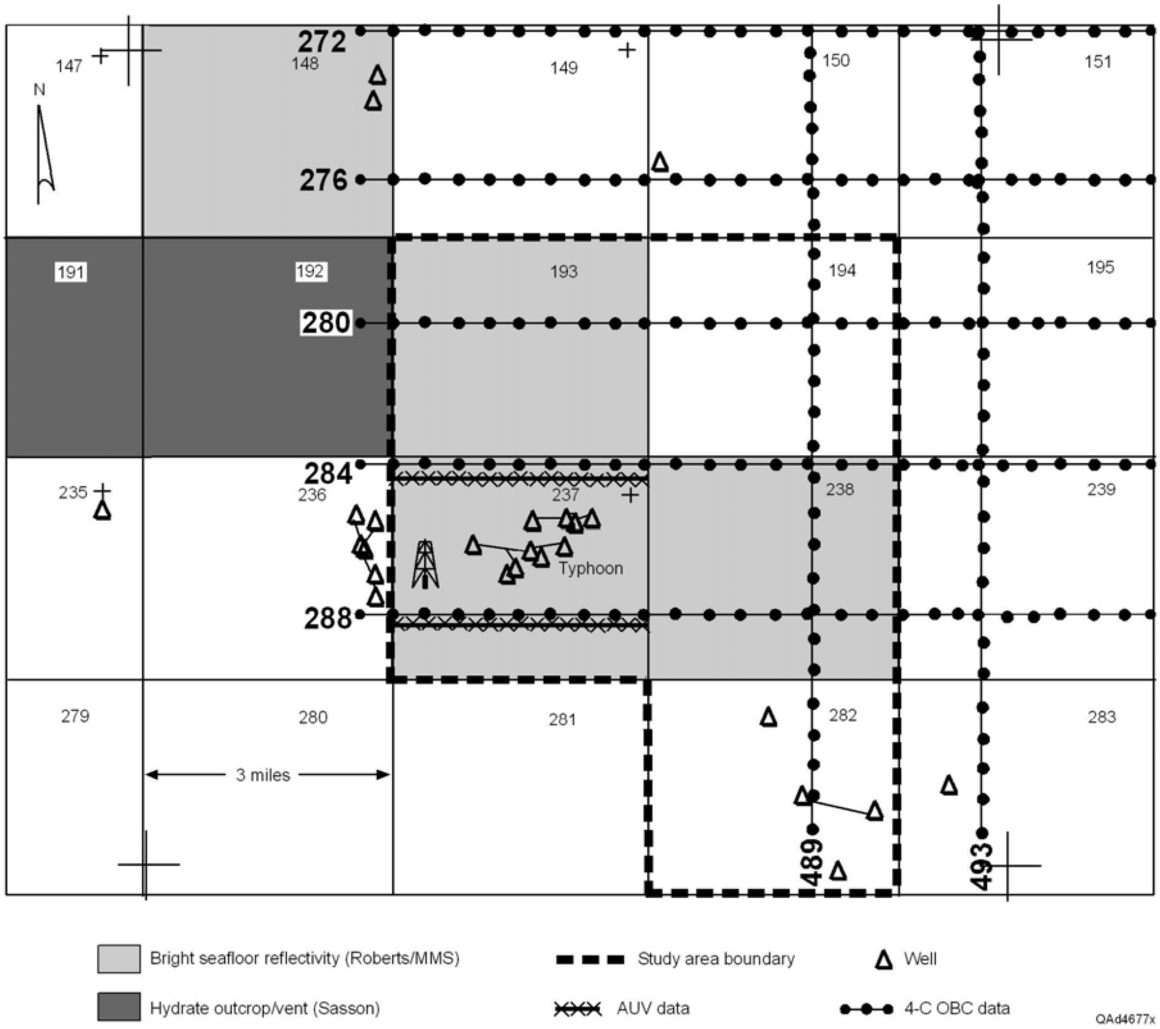

Figure 2. Study Site 1. This area extends across five lease blocks, or 45 mi^2 (115 km^2). AUV and OBC profiles are labeled. Critical calibration data in the form of seafloor borings and geotechnical reports exist at the production platform shown in Block GC237. Conventional well logs across some intervals of the hydrate stability zone are available at a few well locations. Lease blocks are shaded to indicate that hard evidence of hydrates exists within these blocks. The color code indicates that the source of the hydrate evidence is either Roberts (2001) or Sassen and others (1999).

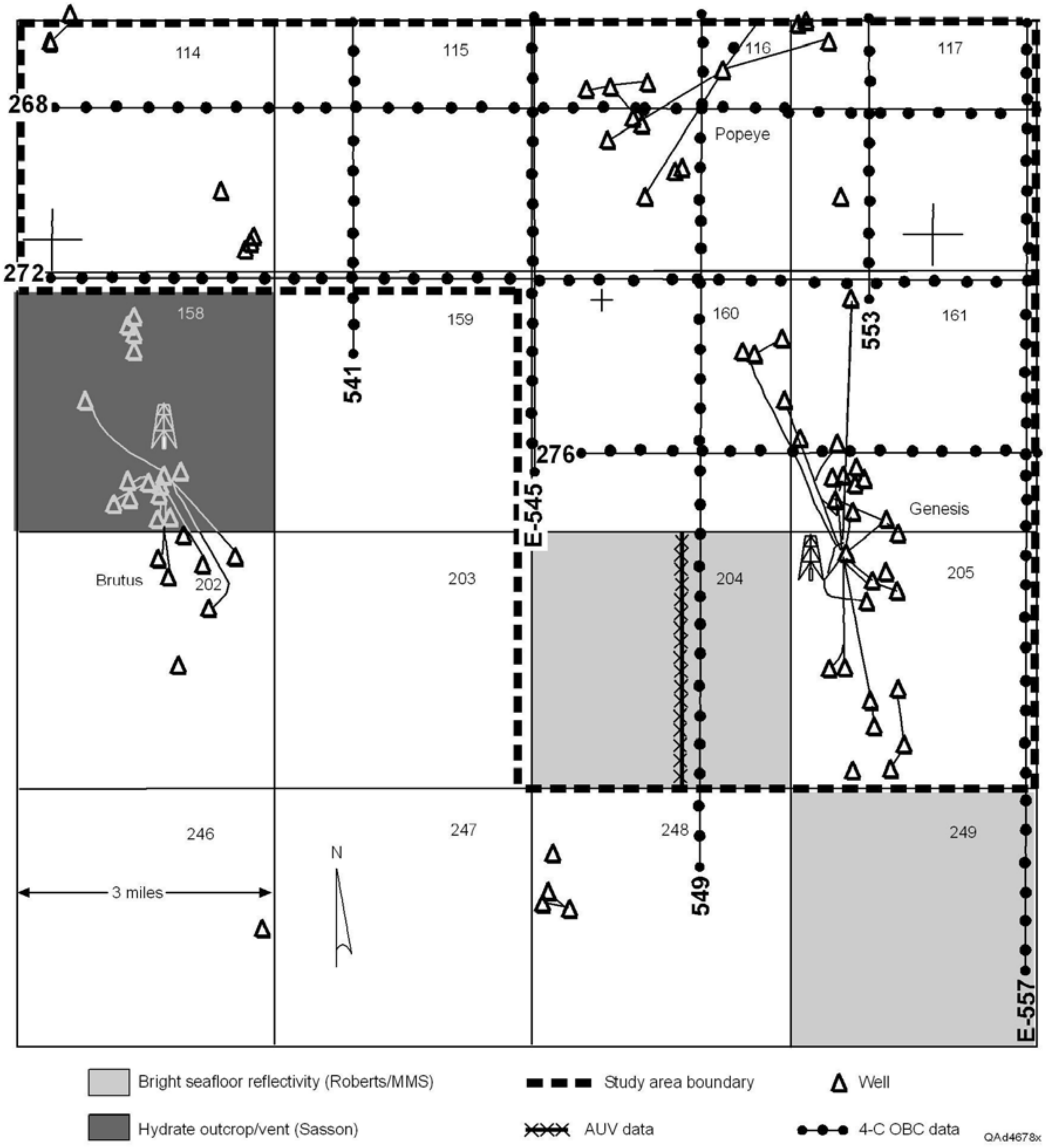

Figure 3. Study Site 2. This area covers eight lease blocks, or 72 mi^2 (184 km^2). AUV and OBC profiles are labeled. Seafloor boring analyses are available as contractor-generated geotechnical reports in Block GC205, where the production platform is shown. Conventional well logs across parts of the hydrate stability zone are available at a few well locations. Lease blocks are shaded to indicate that hard evidence of hydrate exists within these blocks. The color code indicates that the source of the hydrate evidence is either Roberts (2001) or Sassen and others (1999).

As stated in the discussion of Task 3, DOE did not accept the research findings of Roberts, Sassen, and Brooks and Bryant at our two selected study sites as being sufficient evidence that hydrates existed at these two locations and requested a new deliverable and an additional project decision point—a report that presented subseafloor evidence of the existence of hydrate at each study site. To prepare this unplanned deliverable, we expanded our well log database to the offshore lease blocks marked on the map displayed as Figure 4. We did a search of commercial offshore well log databases and found appropriate logs in 53 wells inside these marked lease blocks. We use the term *appropriate* to mean that log data were found that extended across some portion of subseafloor strata within the hydrate stability zone.

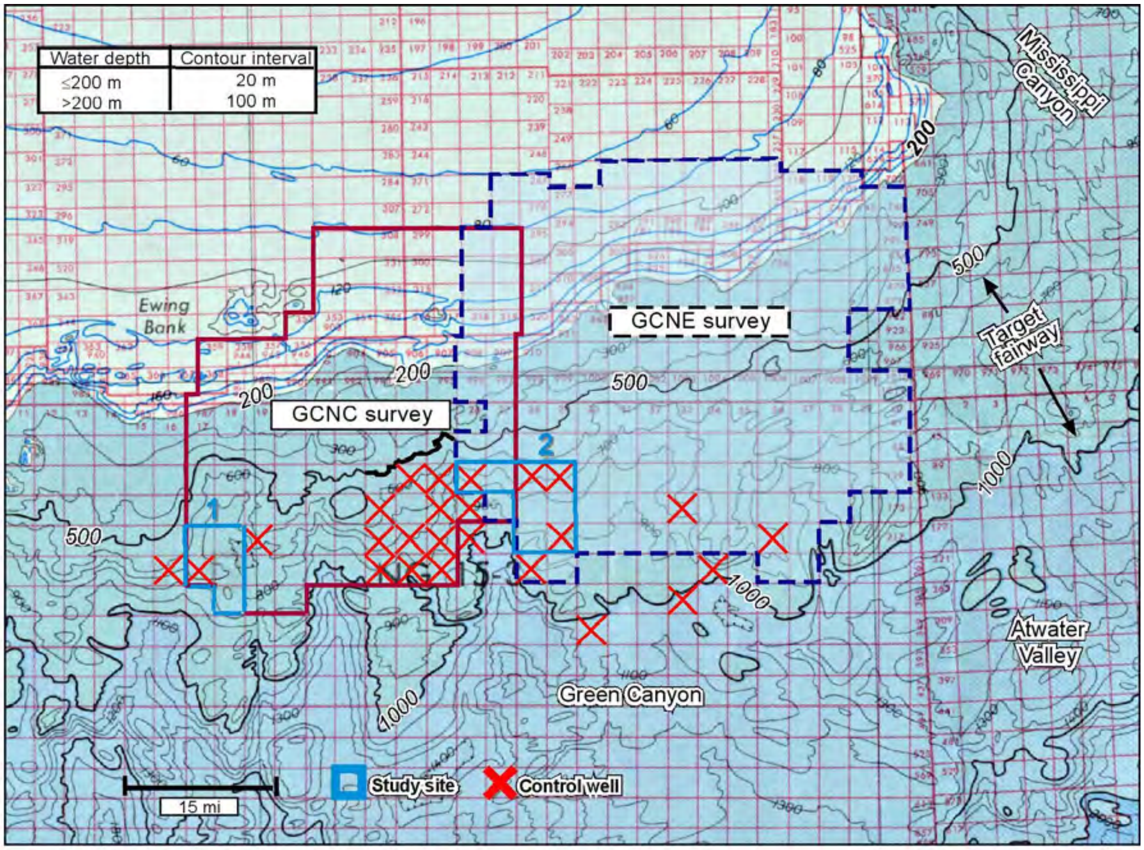

U.S. Department of Commerce (1986)
QAd3453(aaa)x

Figure 4. Map defining locations of **Study Site 1** and **Study Site 2** and critical water-depth contours of 500 and 1,000 m that define the boundaries of the hydrate ***Target fairway*** across the area. Lease blocks where well log data were added to the research database are marked with an ×.

It is difficult to find any wireline-based log data acquired near the seafloor in commercial oil and gas wells in the Gulf of Mexico (GOM) because GOM operators have no economic interest in the shallow near-seafloor interval. After logging-while-drilling (LWD) technology was introduced into GOM operations in the 1990’s, some offshore operators began to collect LWD data immediately after drilling out of surface casing. However, even in wells where LWD data are available, the only logs that are acquired are gamma-ray and resistivity data. As a result, our evaluation of subseafloor evidence of hydrate had to be limited to information provided by only two log curves: gamma-ray and resistivity.

An analysis by Wempe (2000) is particularly germane to any study of the resistivity response of hydrate dispersed in unconsolidated, high-porosity, near-seafloor sediments. A key graphic of Wempe's study is reproduced as Figure 5a. Our modification of this graphic is shown as Figure 5b. In these figures, the horizontal axis is porosity, and the vertical axis is normalized resistivity $\mathbf{R/R_W}$, where R is the resistivity measured across a medium of porosity $\mathbf{\Phi}$, and R_W is the resistivity of the fluid that fills the pores. The interval labeled $\mathbf{\Phi_C}$ defines the range of **critical porosity**, which is porosity in which the grains of a high-porosity medium convert from a suspended state to a load-bearing condition in which each grain touches at least one other grain. Critical porosity varies from about 0.3 for poorly sorted sediments, to approximately 0.4 for well-sorted rounded grains, to almost 0.6 for highly oblate (flat) grains.

The data plotted in Figure 5 are comprehensive and include laboratory measurements and field data gleaned from 11 studies referenced by Wempe (2000). A key concept demonstrated by these data (Fig. 5b) is that the resistivity behavior of all porous media converge to the **Hashin-Shtrikman Lower Bound** (**HS-**) when the porosity of the medium equals or exceeds critical porosity (Hashin and Shtrikman, 1962). Because the porosity of the deep-water, near-seafloor sediments that span the hydrate stability zone in the Green Canyon area of the GOM equals or exceeds critical porosity, we are led to an important conclusion: *the Hashin-Shtrikman Lower Bound is an ideal function for describing the resistivity of deep-water hydrate systems in the GOM.*

The Hashin-Shtrikman Lower Bound that we calculated for our study areas is plotted in Figure 6 to illustrate how the resistivity of deep-water sediment varies as a function of hydrate concentration. As hydrate concentration increases from 0 to 60 percent of the pore space (top horizontal axis of the plot), resistivity increases from approximately 0.6 ohm-m to only 2 ohm-m. The implication is that even with 60 percent of the pore space occupied by hydrate, a large number of connected paths of conductive brine continue to wend through the sediment-hydrate-brine mixture.

Included in Figure 6 is a curve labeled **Archie Equation 1** that describes the resistivity behavior of the clay-free form of the Archie Equation (Archie, 1942) that we think is appropriate for the hydrate systems that we are studying across Green Canyon. Also included is a curve (**Archie Equation 2**) that describes the Archie Equation developed by Collett and Ladd (2000) at Blake Ridge. The difference between the responses of these two Archie Equations is created by different choices for the constants **m** and $\mathbf{R_W}$ used in the equation.

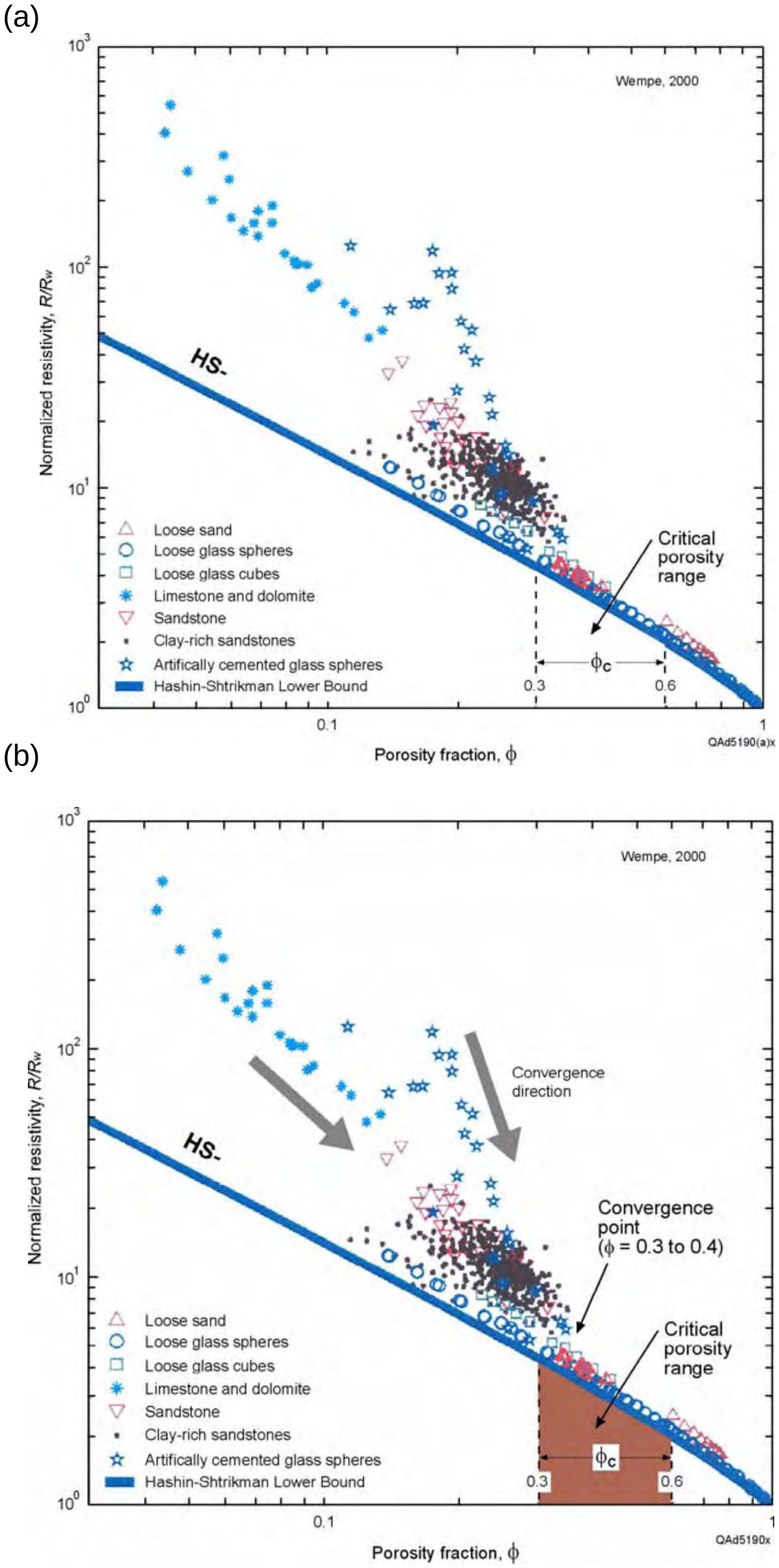

Figure 5. (a) Crossplot of normalized resistivity (R/R_w) and porosity for a large number of laboratory tests and field-data observations that involve a wide range of conductive media (Wempe, 2000). (b) Our modification of the crossplot to emphasize principles important for deep-water hydrate systems. R is measured resistivity; R_w is the resistivity of the pore-filling fluid. The shaded interval Φ_C is the range of critical porosity for grains of different geometrical shapes. Note that all data converge to the Hashin-Shtrikman Lower Bound as porosity increases and enters the critical-porosity range.

We argue that our Archie Equation 1 is correct because it converges to the HS- curve at low hydrate concentrations. In contrast, Archie Equation 2 does not converge to the HS- curve and predicts low, incorrect hydrate concentrations. We consider the use of HS- theory for developing the appropriate mathematical formulation of the resistivity equation that should be used to predict hydrate concentration in high-porosity seafloor sediment to be one of our significant research findings.

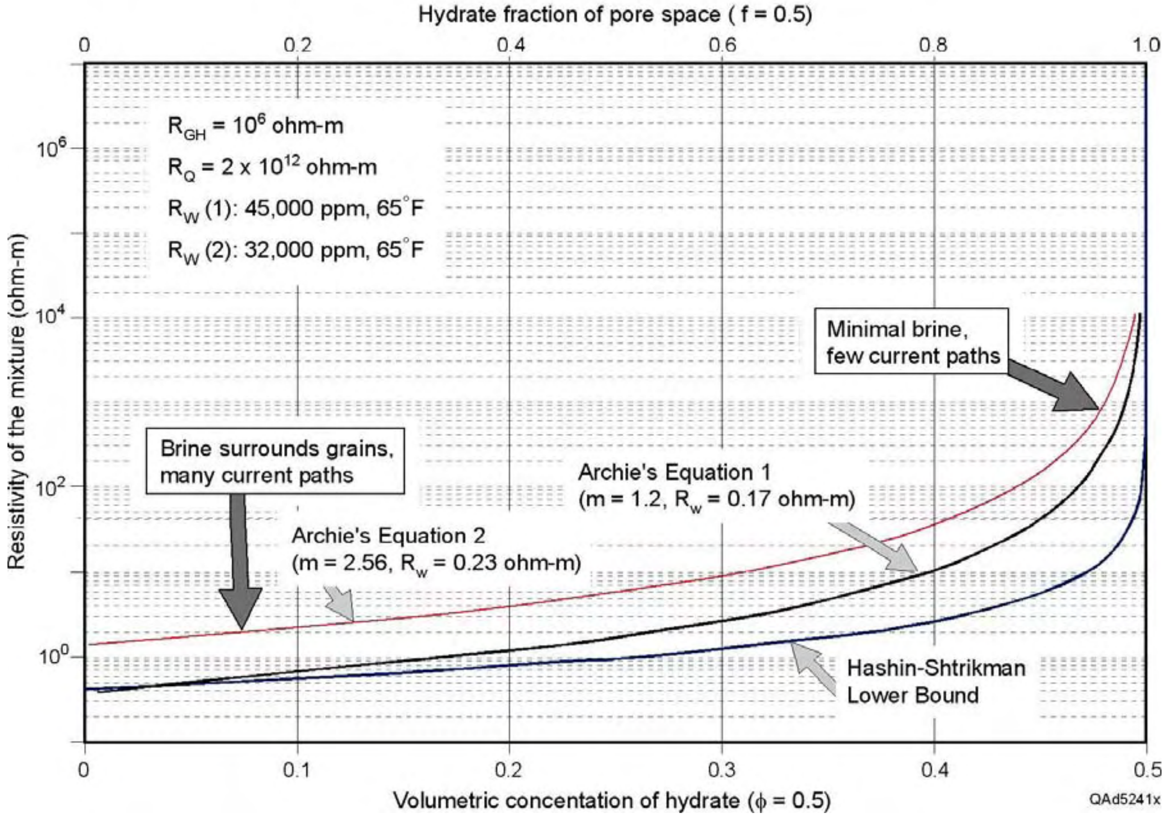

Figure 6. The Hashin-Shtrikman Lower Bound (HS-) and two formulations of the clay-free form of the Archie Equation displayed as functions of resistivity and hydrate fraction. Hydrate fraction is defined in terms of the pore volume (top axis) and the unit volume (bottom axis). Archie Equation 1 is our formulation for deep-water hydrate systems. Archie Equation 2 was proposed by Collett and Ladd (2000). We stress this fundamental principle: any equation used to describe the resistivity of deep-water mixtures of sediment and dispersed hydrate must agree with, or approximate, the Hashin-Shtrikman Lower Bound at low hydrate concentrations, as does our Archie Equation 1. Points **A** and **B** are discussed in the full DOE report that was submitted as the required deliverable for Task 4 (Hardage and others, 2006b).

We used concepts of the Hashin-Shtrikman Lower Bound to define appropriate empirical constants needed for the Archie Equation when that equation is used to analyze deep-water mixtures of sediment, hydrate, and brine. We then applied this formulation of the Archie Equation to the resistivity-log database that we amassed. Gamma-ray and resistivity logs across selected targeted intervals of the hydrate stability zone from two wells drilled at Study Site 2 are displayed in Figures 7 and 8. In each figure, the specific interval over which hydrate concentration was estimated is indicated by the bracket drawn along the right edge of the resistivity curve. Two estimates of hydrate concentration were calculated for each interval. One estimate used the clay-free form of the Archie Equation, and the other used the clay-dependent form of the equation. The **probability distribution function** (**pdf**) of hydrate concentration produced by each form of the Archie Equation is identified in each figure.

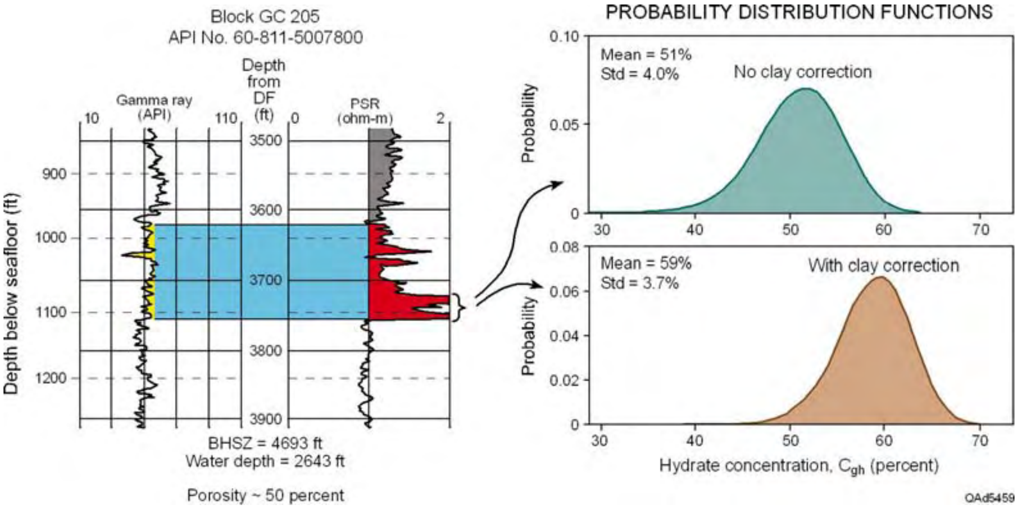

Figure 7. Hydrate concentration calculated across depth interval 3,720 to 3,760 ft at Study Site 1. The upper pdf results when the clay-free form of the Archie Equation is used. The lower pdf results when the clay-dependent form is used. The mean reading of the resistivity log across the bracketed interval is 2 ohm-m. The average porosity is approximately 50 percent.

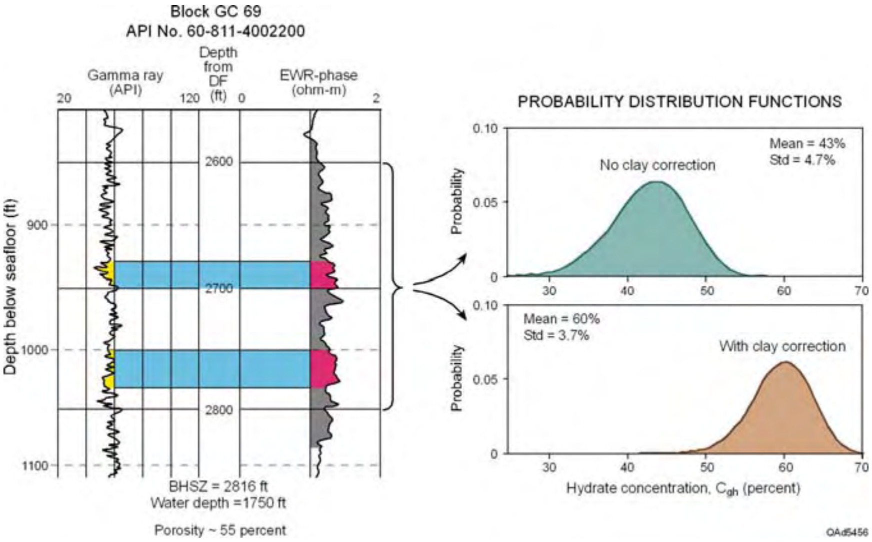

Figure 8. Hydrate concentration calculated across depth interval 2,600 to 2,800 ft at Study Site 2. The upper pdf results when the clay-free form of the Archie Equation is used. The lower pdf results when the clay-dependent form is used. The mean of the resistivity log readings across the bracketed interval is 1.3 ohm-m. The average porosity is approximately 55 percent.

We did estimates of hydrate concentration similar to those illustrated in Figures 7 and 8 at 28 wells within and near our two study sites. The conclusion of this investigation is summarized as the maps in Figures 9 and 10. These maps show resistivity logs indicating that our two study sites are ideal for hydrate research in that each site spans an area of low (no?) hydrate concentration, as well as an area of relatively robust hydrate concentration.

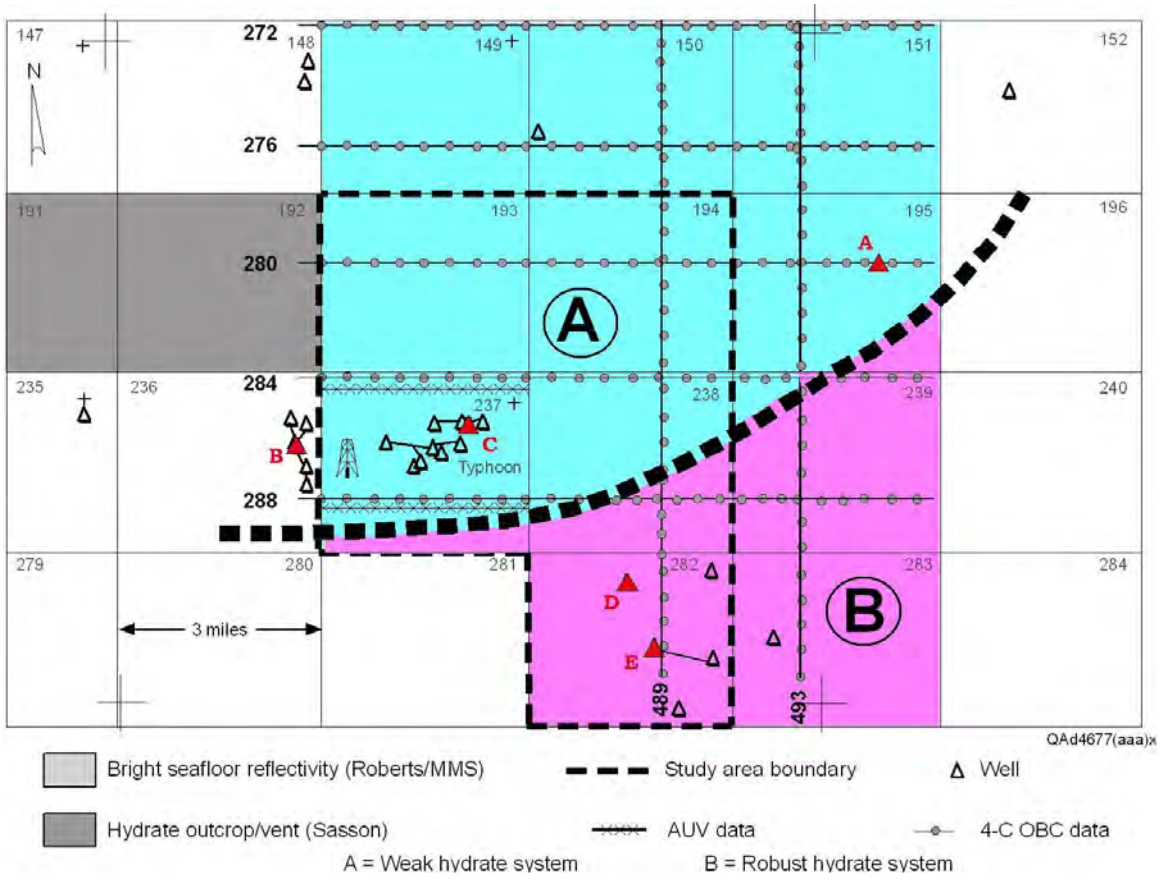

Figure 9. Generalized properties of the hydrate system across Study Site 1 as implied by resistivity logs. The hydrate system can be segregated into two domains, **A** and **B**. Domain **A** has thin hydrate intervals and/or low hydrate concentration. Domain **B** has thick hydrate intervals and several units with high concentrations of hydrate. To support these statements, cross sections illustrating hydrate concentrations were constructed from resistivity logs acquired in the lettered wells marked by red triangles. These cross sections were exhibited in the report that was sent to DOE as the decision-point deliverable for Task 4 (Hardage and others, 2006b).

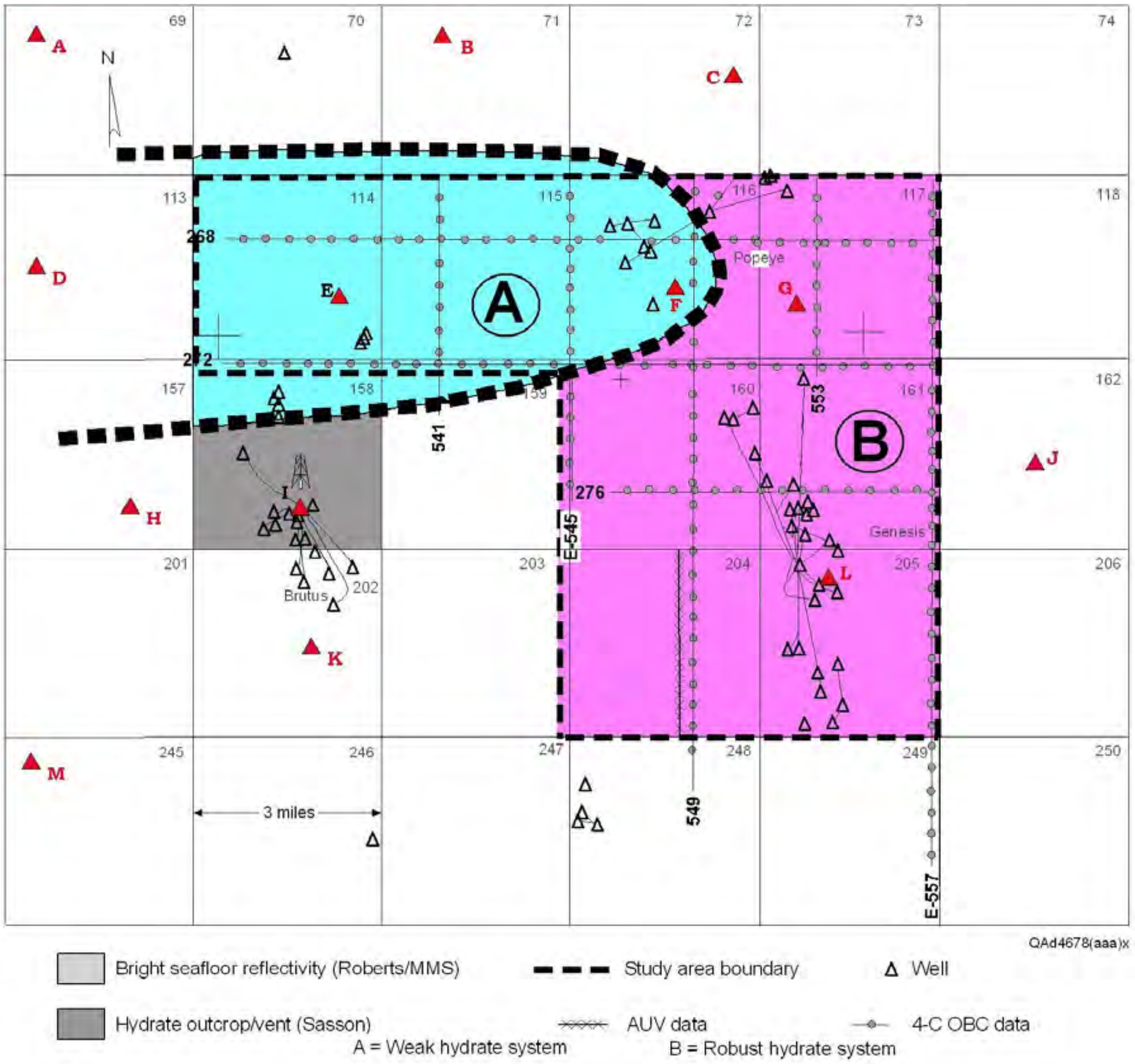

Figure 10. Generalized properties of the hydrate system across Study Site 2 as implied by resistivity log data. The system can be segregated into two domains, **A** and **B**. Domain **A** has thin hydrate intervals and/or low hydrate concentration. Domain **B** has thick hydrate intervals and numerous units with high hydrate concentrations. To support these statements, cross sections illustrating hydrate concentrations were constructed from resistivity logs acquired where the lettered red triangles are plotted. These log displays were provided to DOE as the report deliverable for Task 4 (Hardage and others, 2006b).

DOE accepted the report that was delivered at the conclusion of Task 4 as satisfactory subseafloor evidence of the presence of hydrate at our two selected study sites (Hardage and others, 2006b). Our research team considers this report to be a confirmation of the good-quality research that was done by Roberts and Sassen that caused them to conclude that hydrates existed at the two sites that we selected and a justification of our faith in the reliability of the work done by these two colleagues.

Task 5.0: Produce P-P and P-SV Trace Gathers

In our seismic imaging approach, 4C OBC seismic data are treated as common-receiver gathers, which is basically the same form in which the data are recorded by an ocean-floor sensor system. The 4C data at one typical seafloor receiver station inside one of our study areas are shown in Figure 11. All of our data processing is performed on isolated receiver-station data like the data shown in this figure. Receiver stations are spaced at 25 m along all of the OBC profiles that traverse our study sites (Figs. 2 and 3). Our research team has produced trace-gather displays like that in Figure 11 at approximately 6,000 seafloor stations across our study areas and has examined the responses of all four seismic components to determine whether the gather can be used for imaging purposes. Approximately 10 percent of the station gathers have needed special handling to eliminate problems such as excessive noise, incorrect sensor channel designations, and so forth.

P-P Trace Gathers

The fundamental theory of our data-processing strategy is based on analysis of data that have been acquired using a sensor that has a hydrophone and a vertical geophone. The key sensor-response equations involved in OBC data acquisition are defined and explained in Figure 12. These equations state that after appropriate calibration, a seafloor hydrophone response (**P**) and a seafloor vertical-geophone response (**Z**) can be combined to create downgoing (**D**) and upgoing (**U**) P-P wavefields using the following relationships, expressed in the frequency domain:

(1) $\mathbf{D = P + Z/\cos(\varphi)}$

(2) $\mathbf{U = P - Z/\cos(\varphi)}$.

φ defines the incident angle at which the downgoing compressional wave arrives at the seafloor (Fig. 12).

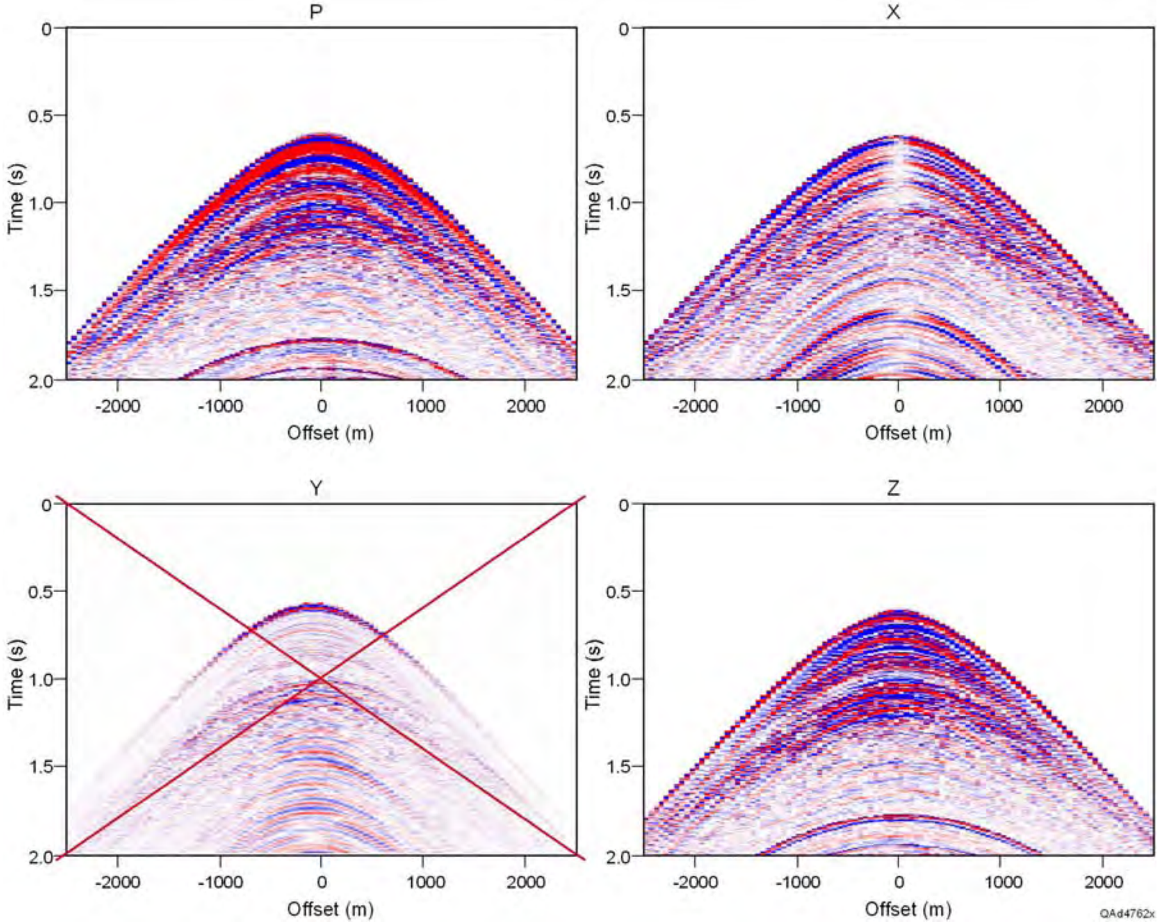

Figure 11. 4C OBC data collected at a single seafloor receiver station. Source spacing is 50 m. The sea-bottom multiple appears at a normal-incidence time of 1.75 seconds. Although this multiple dominates the P-P section when it arrives, we can ignore it because its arrival time is below our gas hydrate target zone. However, the multiple also appears on the **X** (radial) component data and interferes with P-SV reflections arriving between 1.6 and 2 seconds. These P-SV events are in the range of gas hydrate interest, 130 to 200 m below the seafloor. In our 4C OBC data, the crossline **Y** component is generally low amplitude and can be ignored in the normal processing flow. **P** is the hydrophone response; **Z** is the response of the vertical geophone.

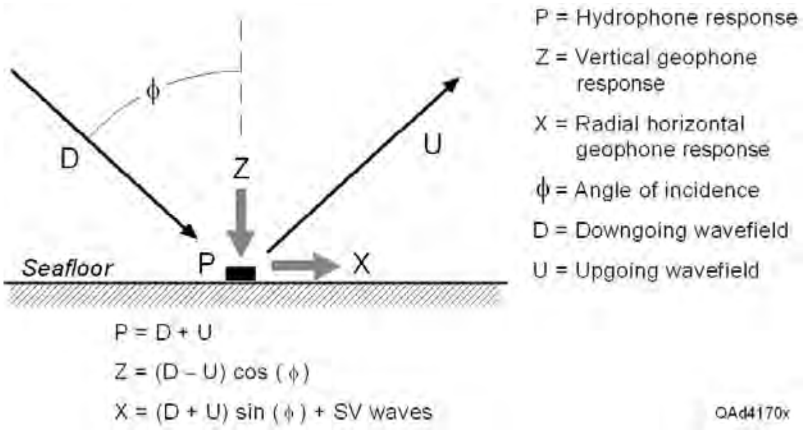

Figure 12. Basic responses of 4C ocean-bottom sensors. The three response equations are keys to our imaging theory. We assume that response of the **Y** (crossline) horizontal geophone can be ignored. This assumption is correct for the data used in this study but needs to be verified at other study sites. A second assumption is that the V_P/V_S velocity ratio is high, positioning the P-to-SV conversion point almost directly beneath the seafloor receiver station. As a result, the upgoing SV raypath is almost vertical, and essentially all of the SV response is on inline horizontal geophone **X**. The SV wavefield can then be separated from the **X** response by calibrating and weighting the **P** response and subtracting it from **X**. We determine the wavefield to subtract from **X** by calculating a constrained cross-equalization filter to change **P** to **X**.

In Figure 13 we show **P**, **Z**, **U**, and **D** waves at a single receiver location. For a better demonstration of the P-P wavefield separation, a static time shift has been applied to flatten the direct arrival (and the ocean-floor reflection). The flat events in the downgoing image appear in all four panels. In this time window we see two of the several air-gun bubble pulses (**B**) that exist in these data. Reflection events appear as smiles. The downgoing wavefield panel **D** shows almost no sign of the reflection events that appear in the other three panels. The upgoing wavefield **U** shows the air-gun bubbles that result when the strong seafloor reflection coefficient convolves with the downgoing wavelet. Note that the vertical geophone **Z** provides a better reflection picture than does the hydrophone **P**. The difference in these two sensor responses occurs because the downgoing wavelet and the seafloor-reflected wavelet combine constructively on the hydrophone and destructively on the geophone (see equations in Figure 12). The P-P wavefield-separation procedure illustrated in Figure 13 has been performed at most of the 6,000 OBC receiver stations involved in the OBC profiles that cross our two study areas.

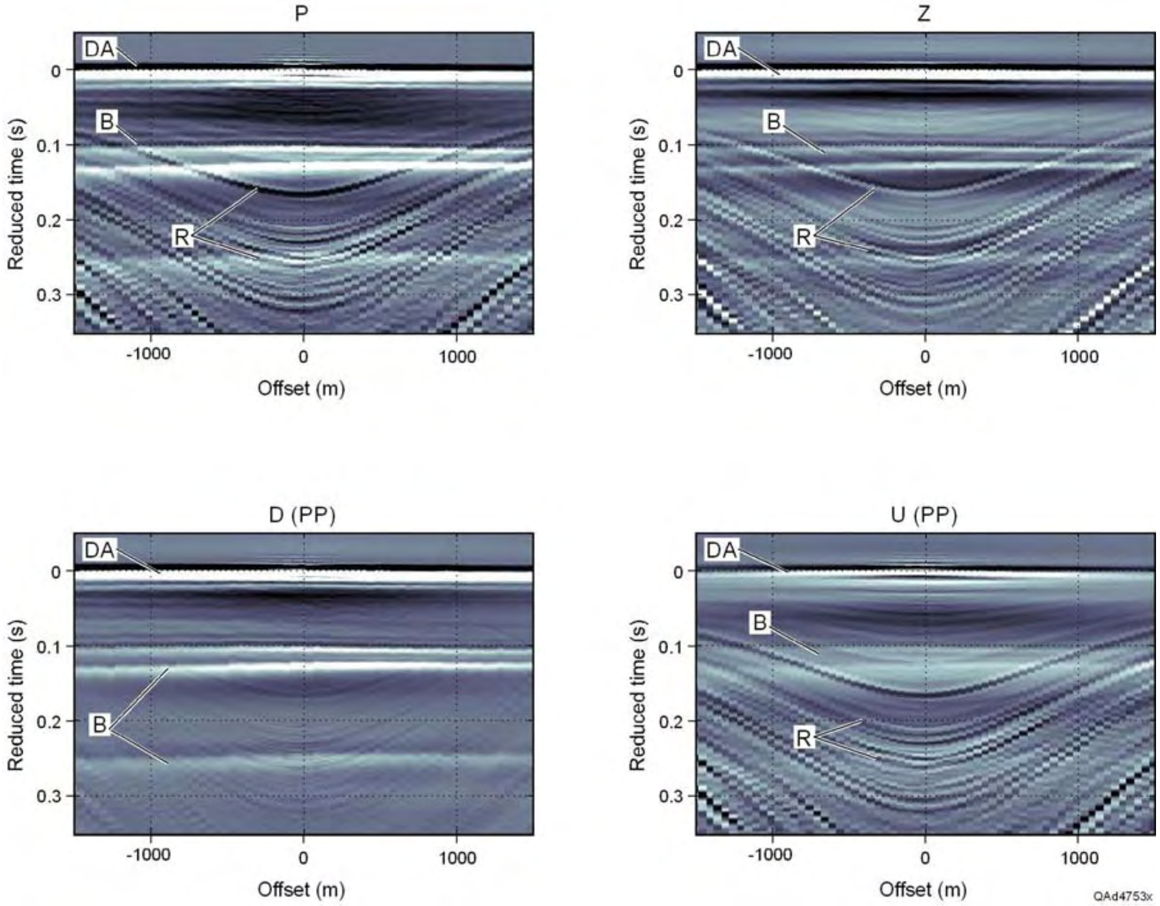

Figure 13. Reduced-time display showing **P**, **Z**, **U**, and **D** waves extending to 0.35 seconds below the seafloor, which is a time interval of interest in our hydrate study. The separation of up- and down-traveling P waves (bottom two panels) is quite good. By taking the ratio of the up-traveling and the down-traveling P waves, we uncover shallow P-P data that are overprinted by air-gun bubbles without stacking the data. For display, these data have been statically corrected to align seafloor reflection and direct arrival at time zero. **DA** is the direct arrival, **B** is an air-gun bubble, and **R** is a P-P reflection.

P-SV Trace Gathers

In Figure 14 we show isolation of the P-SV wavefield using the formulation defined in Figure 12. In this case, calibration of the horizontal geophone **X** with the hydrophone (**P**) is critical to successful P-SV wavefield separation. To accomplish this X-to-P sensor calibration, we first use a single filter that is an average empirical estimate based on P-P reflection data (or on head waves if they are available) to correct the **X** geophone roughly to the hydrophone **P**. We then calculate a cross-equalization filter to change **P** to **X** for each trace. This step must be done judiciously because it is easy to overdo the correction and to eliminate some of the P-SV component, just as when performing conventional, statistically based spiking deconvolution, one can overdo a correction and attenuate (or eliminate) valid reflections.

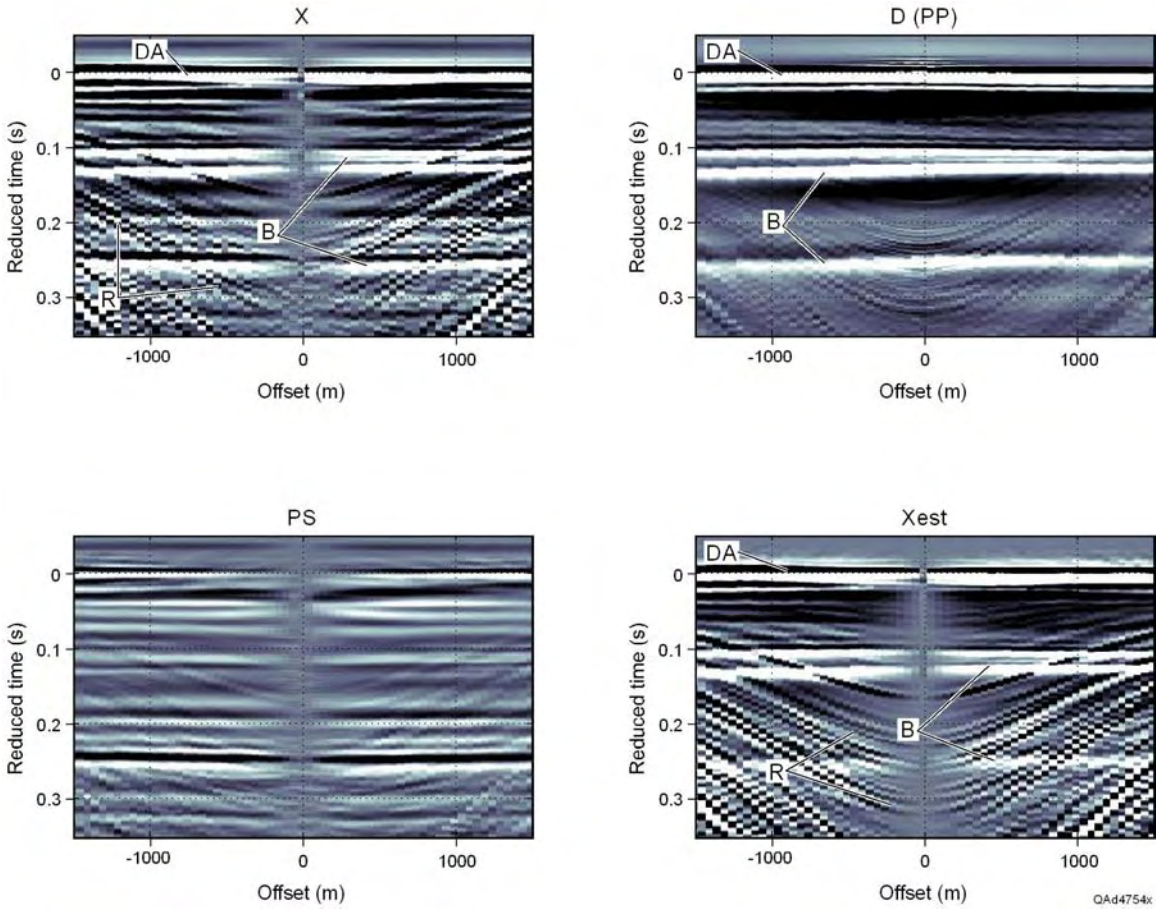

Figure 14. Reduced-time display illustrating isolation of the P-SV wave by combining **P** and **X** data. The radial component **X** in the upper left is superposition of the downgoing P wave (upper right), the upgoing P-P wave (lower right, Fig. 13), and upgoing P-SV reflections (see bottom equation in Figure 12). In the lower right is the result of cross-equalization of **P** to **X**. This wavefield $\mathbf{X}_{\mathbf{est}}$ should contain the downgoing P wavefield (flat events) and upgoing P-P waves (smiles labeled “R”). By subtracting the lower-right panel from the upper-left panel, we obtain the lower-left panel consisting of nearly isolated P-SV reflections (flat) and some residual energy.

A separate cross-equalization is calculated to eliminate the seafloor multiple, which arrives at a different angle than do the direct wave and the shallow P-P reflection data. In Figure 14, all data panels have been corrected to flatten the direct arrival. In the upper-right panel, we show the extracted downgoing P wavefield **D** from Figure 13, which is dominated by air-gun bubbles. The inline **X** component looks like the hydrophone response (upper-left panel of Figure 13) because the **X** sensor is dominated by the flattened downgoing wave and by the P-P reflection events that smile. The lower-right panel above shows the estimate of the **X** component obtained from the hydrophone response by cross-equalization. This estimate $\mathbf{X}_{\mathbf{est}}$ is indeed a good copy of **X**. When we subtract the lower-right panel from the **X** component, we produce the lower-left panel, which shows the isolated P-SV reflection events. These P-SV events have the same flat appearance as that of the direct-wave bubbles. The moveout of these P-SV events is negligible because the V_S velocity is quite low.

This P-SV trace-gather and wavefield-separation process has been done at most of the 6,000 receiver stations that span our two Green Canyon study sites.

Task 6.0: Create P-P and P-SV Images

Calculating Reflectivity

If access is available to downgoing (**D**) and upgoing (**U**) wavefields, subseafloor P-P reflectivity **R** can be recovered by taking the ratio **U/D = R** in the frequency domain, **f**. The inverse Fourier transform of **R(f)** then creates a time-based reflectivity series that starts at the seafloor and extends to a depth that is below the base of the hydrate stability zone. It is this time-based reflectivity **R(t)** that we use to create our high-resolution images of near-seafloor geology.

Figure 15 shows P-P and P-SV reflectivities estimated for a seafloor datum using this wavefield ratio strategy. To obtain this result we first calculate the Fourier transform of the up- and down-traveling waves obtained from the simple combination of raw **P** and **Z** data (Eqs. 1 and 2). At each offset, we divide the up-traveling P-P wave (upper left of Fig. 15) by the down-traveling P wave (lower left, Fig. 13), with a modest damping applied for stability. An inverse Fourier transform then yields the P-P reflectivity result at the upper right in Figure 15. Reduction to seafloor datum is automatic in this process.

To determine reflectivity of the P-SV wave, we follow the same procedure. We divide the extracted P-SV wave (lower left, Fig. 15) by the downgoing P wavefield (lower left, Fig. 13). The result is the P-SV reflectivity shown at the lower right of Figure 15. Because the direct arrival has already been removed, the effect of this deconvolution is less dramatic for P-SV than for P-P.

For both reflectivities (P-P and P-SV), we can follow reflection events out to large source offsets corresponding to local incident angles exceeding 60°. At this stage of data processing, both P-P and P-SV data are suitable for detailed isolation and analysis of individual reflection events.

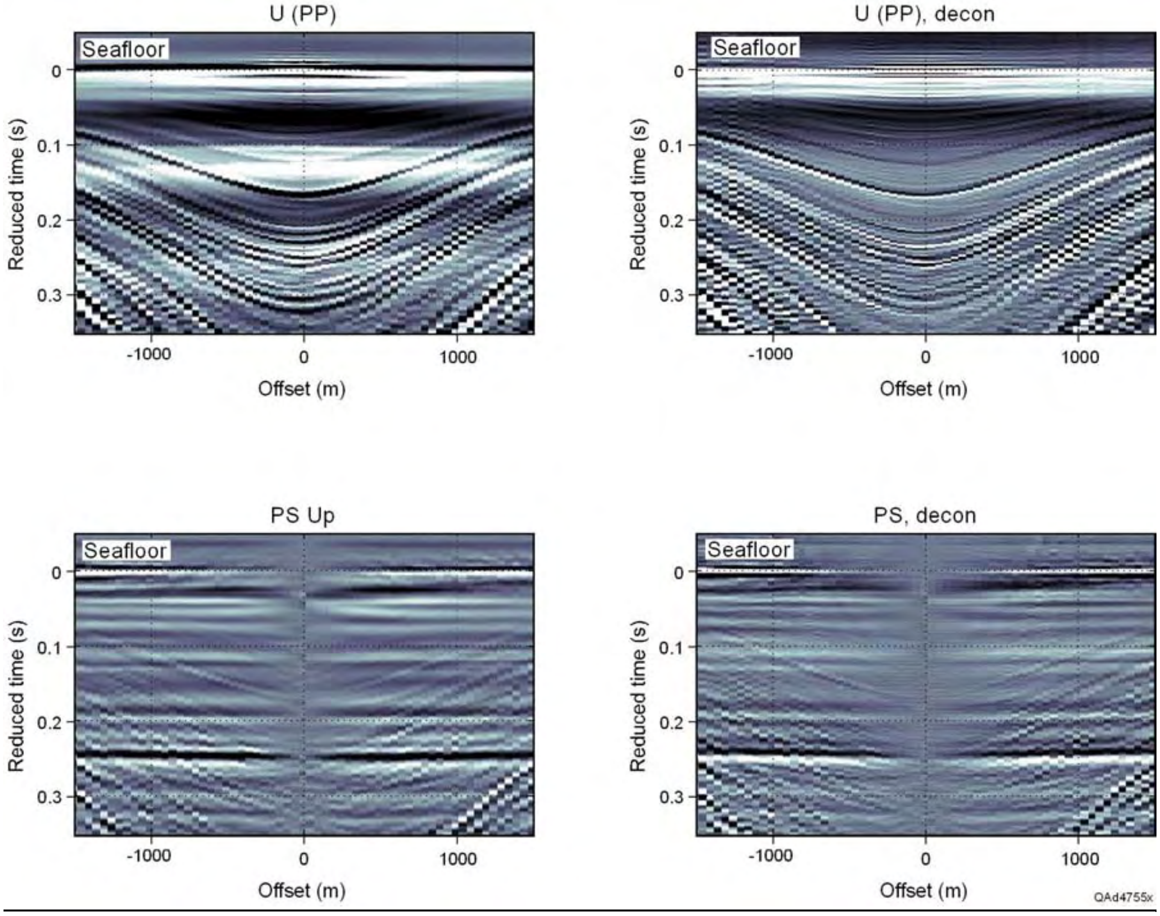

Figure 15. Upgoing P-P and P-SV waves are shown on the left. Deconvolution with the downgoing **P** wave produces the reflectivity panels on the right. The upper-right display is P-P reflectivity; the lower-right display is P-SV reflectivity.

To create P-P and P-SV images, we apply dynamic corrections to our reflectivity estimates to correct for the small moveout on the near-offset traces. In Figure 16, we show the deconvolved P-P data (that is, the P-P reflectivity) from Figure 15 for the full ±2,500-m offset range after applying a time differentiation to enhance frequency of the data. The data are excellent quality over the full offset range. Raytracing with a layered-velocity model of subseafloor geology is then used to calculate curves of source-receiver offset versus time that correspond to reflection depth points that are a fixed offset distance from the receiver location. Examples of these raytrace curves calculated for this common-receiver station are shown as Figure 17 for offsets starting at ±10 m and increasing at 25-m intervals out to ±160 m. Data can now be recovered by interpolation along these curves to produce seismic image traces at specified depth-point offsets from the receiver location.

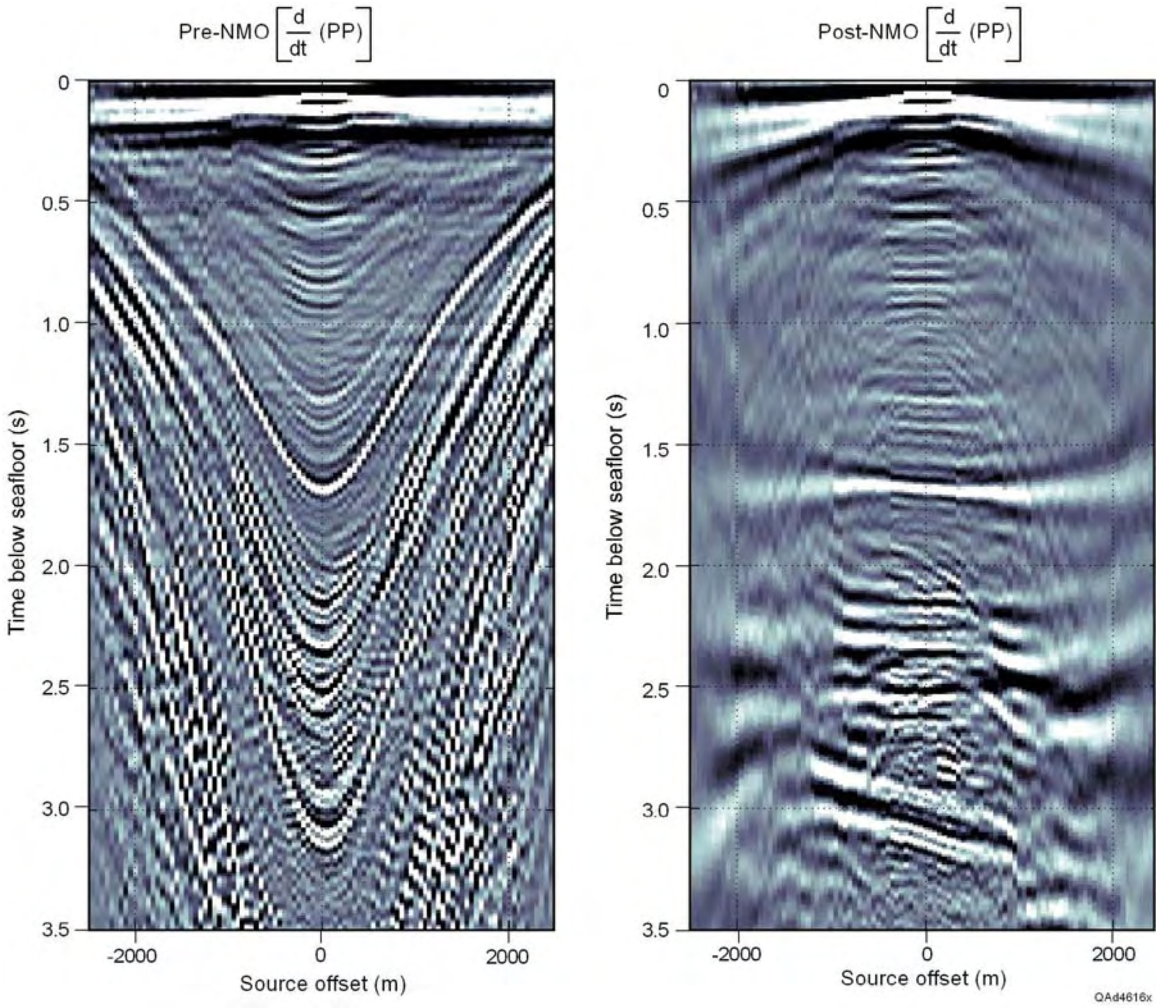

Figure 16. After time differentiation, P-P reflectivity for a single common-receiver gather is shown on the left. The data used here are the data displayed as the upper-right panel of Figure 15. The same data are shown on the right after dynamic time correction. The full source-receiver offset range (±2,500 m) is shown. Extreme moveout stretch at large source offsets is apparent.

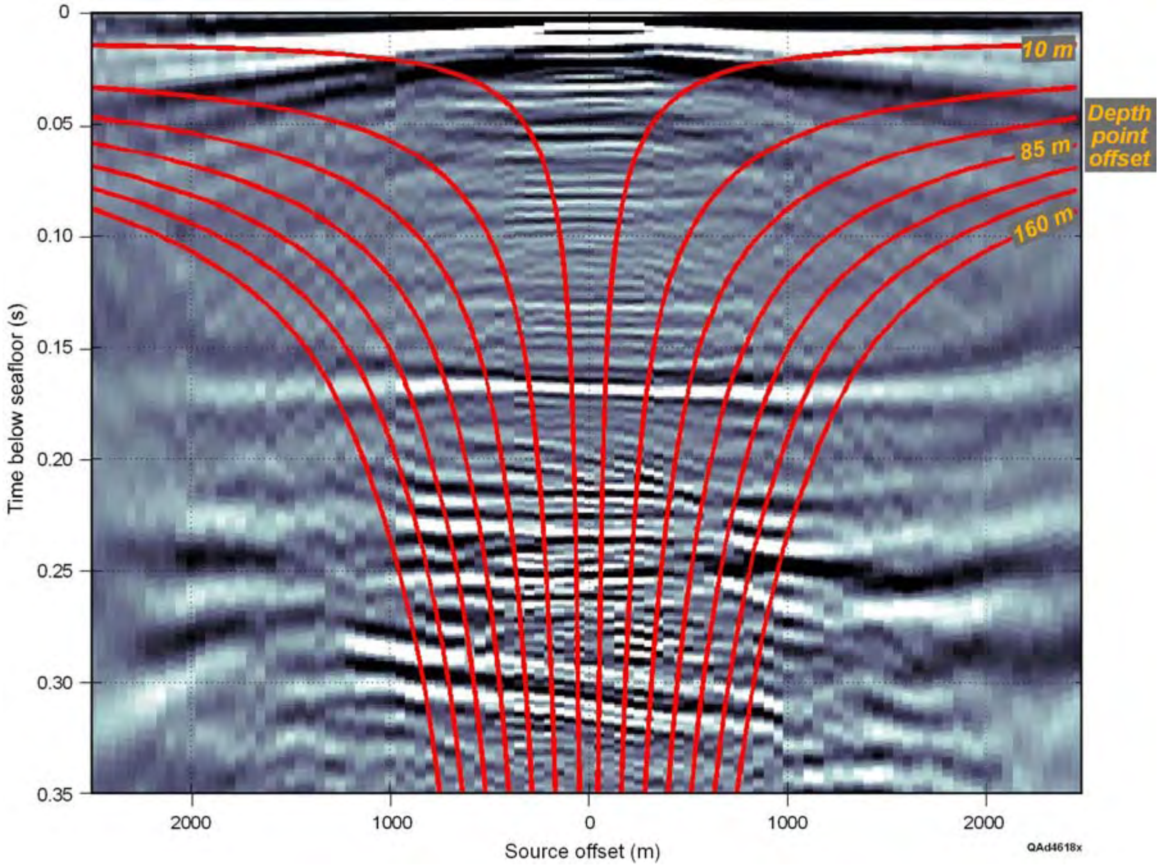

Figure 17. P-P reflectivity after application of raytrace-based, dynamic time corrections calculated for a flat-layered Earth model. Red lines define the location of image-trace data at fixed depth-point offsets from the receiver location. Depth-point-offset curves are shown for offsets of ±10 to ±160 m at 25-m intervals.

In Figure 18, we show the full deconvolved P-SV common-receiver gather, before and after dynamic corrections. These data are the subseafloor P-SV reflectivity at this same OBC receiver station. Note that even before dynamic moveout corrections, the P-SV events are nearly flat, so a limited-range stack before applying a dynamic moveout correction can provide a fairly good P-SV image. The depth-point-offset curves overlain on the P-SV reflectivity show that for our OBC data, any P-SV image trace of near-seafloor geology will extend only 1 or 2 m away from a receiver station.

When these data-processing steps are followed at all receiver stations along an OBC profile, a series of miniscale P-P and P-SV images is created at each receiver station, Each mini-image represents the subseafloor image across a 25-m distance, which is the receiver-station interval for the OBC data that we analyze. We then combine these small-scale images to make continuous P-P and P-SV images that extend for several kilometers along each OBC profile. Our P-P image can have a trace spacing of 1 or 5 m across this 25-m receiver-to-receiver interval. In contrast, our P-SV image can have only a single image trace positioned exactly at each receiver station, meaning that the trace spacing of our P-SV image is the same as the receiver-to-receiver interval along the profile.

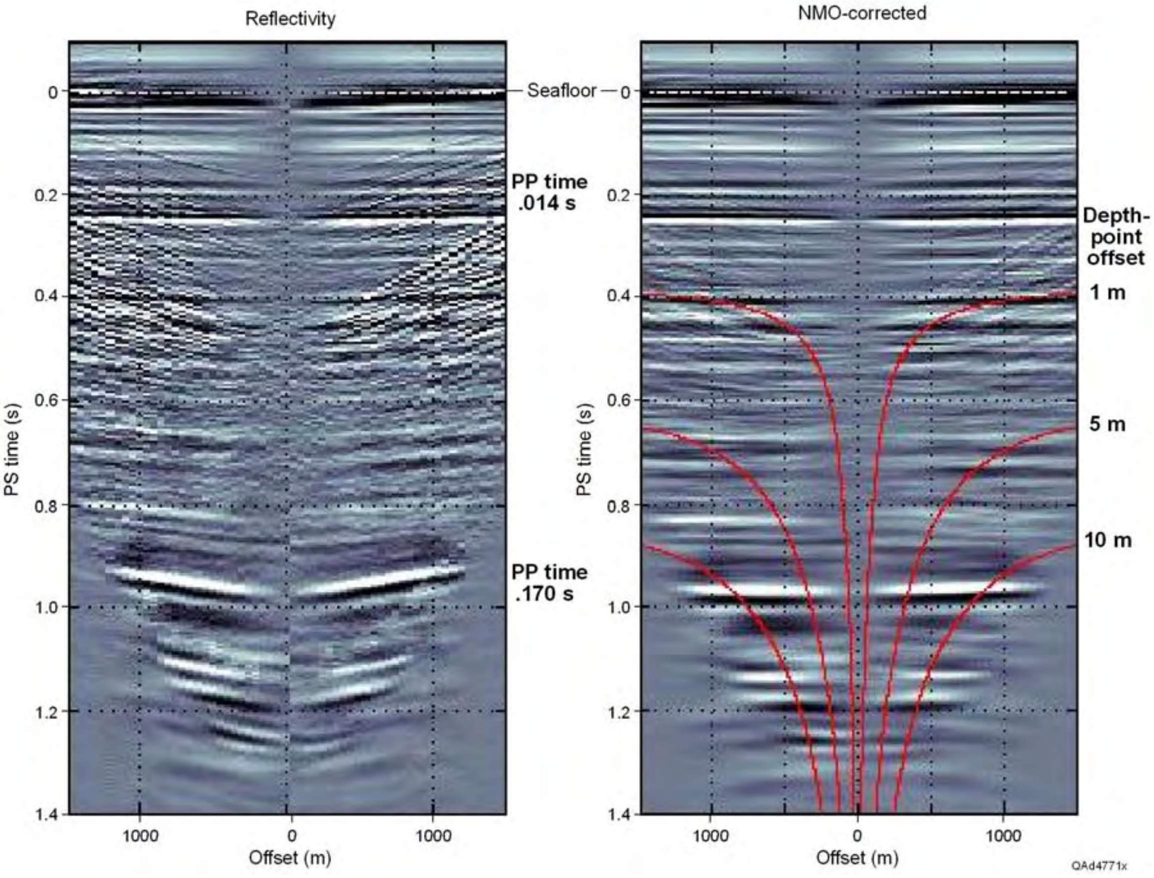

Figure 18. P-SV reflectivity before and after dynamic moveout correction. A five-trace mix was applied on the right panel. 1-m, 5-m, and 10-m depth-point offset lines are shown in red on the right. P-P strong reflector times of .014 and .170 seconds are shown at depth-equivalent P-SV times of .25 and .98 seconds.

Comparison with VSP Imaging

The image processing of a 4C OBC common-receiver gather can be compared with the image processing of a vertical seismic profile (VSP), where reflection information is recovered from strata immediately beneath the VSP vertical array. In a VSP, we rarely have a hydrophone in the downhole receiver stations. Instead, the separation of up- and down-traveling waves is accomplished by processing data acquired using a vertical array of 3C geophones. Use of the down-traveling wave as the wavelet for the VSP deconvolution process is analogous to the approach we use here. Our approach to dynamic correction and recovery of a set of traces at several fixed offsets from a seafloor receiver station is also similar to the traditional VSP-to-CDP transform used for offset VSP sources. In either case (deep-water OBC data or deep-well

VSP data), we have a great disparity between the lengths of the raypath from source to target and the raypath from target to receiver. For those knowledgeable in VSP data processing, particularly the processing of walkaway VSP data, this comparison may be helpful in understanding the OBC data-processing approach used here. Unfortunately, in VSP applications, we do not have a line of wells at 25-m intervals like we have with our deep-water receivers in the OBC profiles across our study areas.

Task 7.0: Interpret Pre-Stack and Post-Stack Data

Approximately one-third of Task 7 was scheduled to be done by the close of the first half of the study. The remaining two-thirds of the task is to be done during the second half of the project period if the project is continued by DOE. We are on schedule for completing this task. We show as Figures 19 and 20 examples of interpreted post-stack data along one OBC profile that traverses Study Site 2. The P-P and P-SV horizons shown in these two illustrations are preliminary interpretations of depth-equivalent geology in P-P image space and in P-SV image space. We will next do our pre-stack interpretation of the data along this profile in which we will raytrace P-P and P-SV reflection arrival times through a layered velocity model of the subseafloor geology and adjust layer thicknesses and interval velocities until we achieve convergence of these raytrace times and actual P-P and P-SV reflection times observed in our pre-stack common-receiver gathers. This raytracing exercise will require considerable time and energy during the second half of the study.

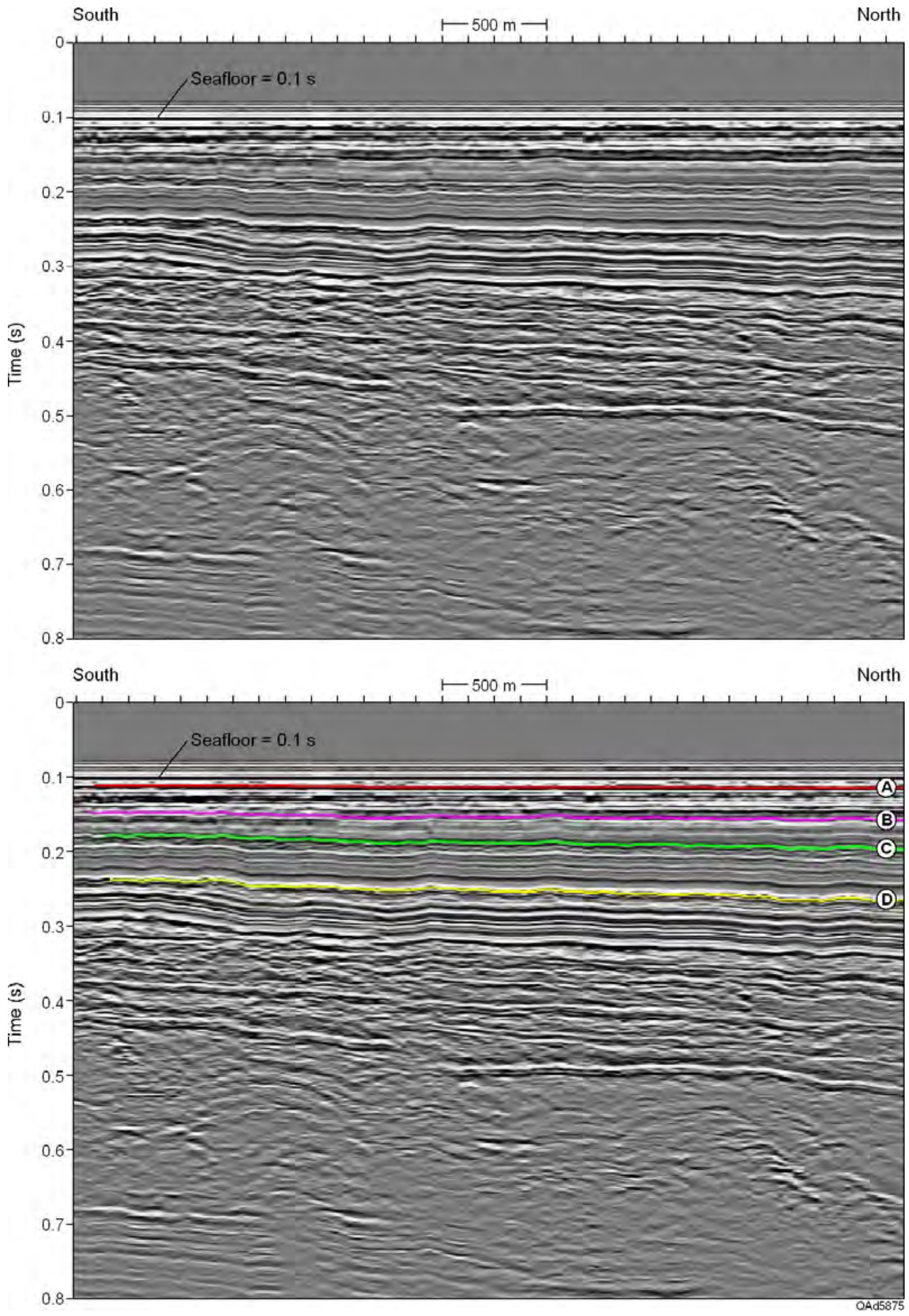

Figure 19. P-P image constructed along the southernmost 4 km of OBC profile 545 that traverses Study Site 2 (Fig. 3). (Top) Basic P-P image. (Bottom) Preliminary stratigraphic interpretation of key stratigraphic intervals. Horizons A, B, C, and D are preliminary interpretations that will be used to build a layered geological system across this hydrate-bearing area. Positions of these horizons will be modified as we proceed with our pre-stack raytrace-modeling approach that defines depth-equivalent P-P and P-SV geology.

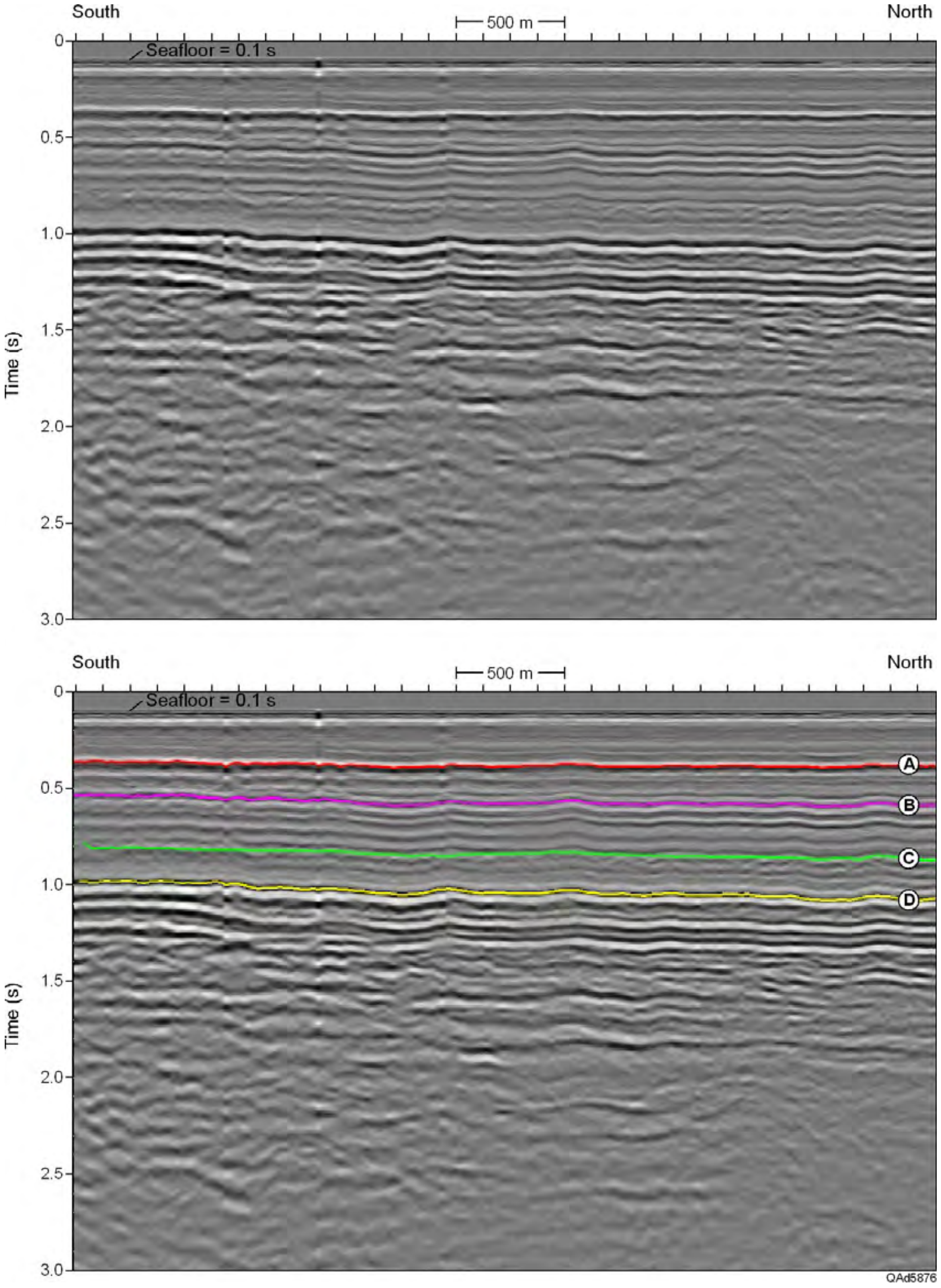

Figure 20. P-SV image constructed along the southernmost 4 km of OBC profile 545 that traverses Study Site 2 (Fig. 3). (Top) Basic P-SV image. (Bottom) Preliminary stratigraphic interpretation of key stratigraphic intervals. Horizons A, B, C, and D are preliminary interpretations that will be used to build a layered geological system across this hydrate-bearing area. Positions of these horizons will be modified as we proceed with our pre-stack raytrace-modeling approach to define depth-equivalent P-P and P-SV geology.

Task 8.0: Select Rock Physics Model

We have converged on the rock physics theory that we will use to associate hydrate concentration with interval values of P and S seismic velocities. An explanation of this theory has been accepted for publication in the AAPG Hedberg Hydrate Conference Publication. A summary of some of the results of the theory appears in *The Leading Edge* (Sava and Hardage, 2006). Rather than describing our work on this task in this continuation report, we will send DOE a separate report that discusses this rock physics theory. This separate report will be the required deliverable that is described in the Statement of Work for Task 8.

Budget and Justification

The budget for the second half of the project (September 1, 2007, through February 28, 2009) is attached. We request no alteration of the funding that we proposed at the start of the project. This budget is identical to the budget in our original proposal for the last 18 months of the study.

One way to view the cost justification for the tasks that will be done is to consider only labor and effort associated with construction of a P-P and a P-SV image of near-seafloor geology that will be done to complete Task 6. As explained in the preceding discussion of Task 6, our imaging strategy for each common-receiver gather is equivalent to constructing a miniscale walkaway VSP image from each P-P and each P-SV trace gather at each OBC receiver station. There are approximately 6,000 receiver stations in the OBC profiles that traverse our two study areas, meaning that we will create approximately 6,000 P-P walkaway VSP images and approximately 6,000 P-SV walkaway VSP images in completing Task 6. To appreciate the magnitude of this task, note that a major VSP data-processing contractor such as Schlumberger or VSFusion will process fewer than 100 walkaway VSPs in a year. The research effort required to complete Task 6 alone will be immense.

Continuation Plans

We do not plan to deviate from the Statement of Work that was agreed to for Tasks 7 through 12 at the start of the project.

Conclusions

Our research team has completed all tasks scheduled for the first half of this project and has produced all deliverables that have been required. We have already published some of our research findings, and one of these publications, the paper by Backus and others (2006), has been awarded *Best Paper in The Leading Edge* by the Society of Exploration Geophysicists (SEG). We are confident that the research findings that we have made in the first half of this project, and which are summarized here, are reliable and important. The SEG publication award from our society of peers is one acknowledgement of the value of our work. We request a continuation of DOE funding so that we can complete our study and publish additional research findings that can benefit others seeking to evaluate deep-water hydrate systems.

References

Archie, G. E., 1942, The electric resistivity log as an aid in determining some reservoir characteristics: AIME Transactions, v. 46, p. 54.

Backus, M. M., Murray, P. E., Hardage, B. A., and Graebner, R. J., 2006, High-resolution multicomponent seismic imaging of deep-water gas-hydrate systems: The Leading Edge, v. 25, p. 578-596.

Brooks, J. M., and Bryant, W. R., 1985, Geological and geochemical implications of gas hydrates in the Gulf of Mexico: Final report, Department of Energy, Morgantown Energy Technology Center, 131 p.

Collett, T. S., and Ladd, J., 2000, Detection of gas hydrate with downhole logs and assessment of gas hydrate concentrations (saturations) gas volumes on the Blake Ridge with electrical resistivity log data, *in* Paull, C. K., Matsumoto, R., Wallace, P. J., and Dillon, W. P., eds., Proceedings of the Ocean Drilling Program, scientific results, v. 164, p. 179-191.

Hardage, B. A., Murray, P. E., and Sava, D. C., 2006a, Assessment of hydrate evidence across the study area: Phase 1 Report for DOE/NETL project DE-PS26-05NT42667, Combining multicomponent seismic attributes, new rock-physics models, and in situ data to estimate gas-hydrate concentrations in deep-water, near-seafloor strata of the Gulf of Mexico: The University of Texas at Austin, Bureau of Economic Geology.

Hardage, B. A., Murray, P. E., and Sava, D. C., 2006b, Log-based evidence of hydrate across Green Canyon study sites: Phase 2 Report for DOE/NETL project DE-PS26-05NT42667, Combining multicomponent seismic attributes, new rock-physics models, and in situ data to estimate gas-hydrate: The University of Texas at Austin, Bureau of Economic Geology.

Hardage, B. A., Murray, P. E., and Sava, D. C., 2006c, Research database: Phase 1 Report for DOE/NETL project DE-PS26-05NT42667, Combining multicomponent seismic attributes, new rock physics models, and in situ data to estimate gas-hydrate concentrations in deep-water, near-seafloor strata of the Gulf of Mexico: Phase 1 report of DOE award DE-PS26-05NT42405: The University of Texas at Austin, Bureau of Economic Geology.

Hashin, Z., and Shtrikman, S., 1962, A variational approach to the theory of the effective magnetic permeability of multiphase materials: Journal of Applied Physics, v. 33, no. 10, p. 3125-3131.

Roberts, H. H., 2001, Fluid and gas expulsion on the northern Gulf of Mexico continental shelf—mud-prone to mineral-prone responses: Geophysical Monograph, 124, p. 145-161.

Sassen, R., Joye, S., Sweet, S., DeFreitas D., Milkov, A., and McDonald, I., 1999, Thermogenic gas hydrates and hydrocarbon gases in complex chemosynthetic communities—Gulf of Mexico continental slope: Organic Geochemistry, v. 30, p. 485-497.

Sava, D., and Hardage, B. A., 2006, Rock physics characterization of hydrate-bearing deep-water sediments: The Leading Edge, v. 25, p. 616-619.

Wempe, W., 2000, Predicting flow properties using geophysical data—improving aquifer characterization: Stanford University, Ph.D. dissertation.

Acronyms and Abbreviations

4C: four-component
AUV: autonomous underwater vehicle
D: downgoing wave mode
HS-: Hashin-Shtrikman Lower Bound
LSU: Louisiana State University
MWD: measurement while drilling
OBC: ocean bottom cable
P: either (1) a compressional wave or (2) a hydrophone response
pdf: probability distribution function
P-P: seismic mode involving downgoing and upgoing P waves
P-SV: seismic mode involving a downgoing P wave and an upgoing SV wave
R: either (1) reflectivity of a seismic mode or (2) electrical resistivity
R_W: electrical resistivity of the fluid filling the sediment pores
SV: converted shear wave
X: horizontal inline geophone
Y: horizontal crossline geophone
Z: vertical geophone
Φ: porosity
Φ_C: critical porosity